

## A novel flow sensing and controlling system based on the flapping film triboelectric nanogenerator toward smart factories



Xiangyi Wang<sup>a,c,1</sup>, Chuanqing Zhu<sup>a,1</sup>, Mengwei Wu<sup>b,1</sup>, Jialin Zhang<sup>a</sup>, Pengfei Chen<sup>c</sup>, Hao Chen<sup>a</sup>, Chenxing Jia<sup>a</sup>, Xiao Liang<sup>a</sup>, Minyi Xu<sup>a,\*</sup>

<sup>a</sup> Marine Engineering College, Dalian Maritime University, Dalian 116026, China

<sup>b</sup> College of Engineering, Peking University, Beijing 100871, China

<sup>c</sup> School of Nanoscience and Technology, University of Chinese Academy of Sciences, Beijing 100049, China

### ARTICLE INFO

#### Keywords:

Triboelectric nanogenerator  
Flapping film  
Smart factory  
Flow sensing  
Flow controlling

### ABSTRACT

In smart factories, it is important to sense and control fluid flows. This study proposes a flow sensing and controlling system based on a flapping film triboelectric nanogenerator (FF-TENG) to sense and control fluid flows in a smart factory. The FF-TENG comprises a soft fluorinated ethylene propylene (FEP) film installed on the central plane of a square tube nozzle. Two copper electrodes are attached to the square tube. When air flows through the nozzle, the flapping FEP film, which periodically contacts the upper and lower electrodes, produces electrical signals. The flow field downstream of the nozzle is significantly influenced by the flapping film. A flow sensing and controlling system can serve as both a flow sensor and a flow controller. The electrical signals generated can indicate the state of the film and can be used to trigger a stepper motor to change film position. Once the film starts flapping, the flow field downstream from the nozzle becomes controllable. The electrical and flow performances of the flow sensing and controlling system have been studied. The experimental results reveal that the proposed system can sense and control the flow in production processes as well as in air conditioning and refrigeration systems.

### 1. Introduction

With rapid industrial development, the demand for intelligent industrial production is increasing [1]. The development of smart factories can improve industrial production efficiency and enable energy savings [2]. However, the currently available industrial sensors have several disadvantages, such as high cost, complex structures and poor adaptability [3–7]. These disadvantages will significantly hamper the pace of smart factory development. Therefore, there is an urgent need for a simple, low-cost and adaptable system that can sense and control fluid flow fields to enable the expeditious development of smart factories [8].

In recent years, triboelectric nanogenerators (TENGs) have been developed as a promising technology; they can convert mechanical motion into electrical signals with high sensitivity, fast response and conformity to mechanical motion [9,10]. Thus, based on the TENG technology, the inductive signals generated by mechanical movements can be used to activate devices [11] and mechanical energy harvested from the surrounding environment can be used to power self-powered

devices [12]. Recently, flexible films and fluid-structure coupled devices based on the principle of TENGs have attracted the attention of many researchers. The films and devices can generate triboelectric signals in two ways: 1) by making an insulating film to press on a metal electrode to achieve contact separation and 2) by making use of the friction between the multiple layers of different types of materials. Both methods can be used to collect wind energy and judge wind speed and direction [13–24]. However, the former method has the advantages of high accuracy and a large measurement range for sensing. The film also affects the flow field while capturing flow energy.

When a fluid flows across a film surface, the differential pressure across the film induces the film to flap. The fluid is driven to produce large-scale oscillations, which facilitate fluid mixing. Recent studies by Xu et al. have revealed that the installation of a flexible film at a jet nozzle outlet can cause self-excited oscillations in the main body of the jet, thereby significantly enhancing its ability to entrain and mix the surrounding fluid [25,26]. Although the flexible flapping film can disturb the fluid, the change in the differential pressure across the film

\* Corresponding author.

E-mail address: [xuminyi@dlmu.edu.cn](mailto:xuminyi@dlmu.edu.cn) (M. Xu).

<sup>1</sup> Xiangyi Wang, Chuanqing Zhu, and Mengwei Wu contributed equally.

caused by flapping is small and can be ignored [27]. They also investigated the variation of the flapping frequency and mixing capacity with film length and found that a change in the film length significantly affected the mixing effect.

In the present study, flow sensing and controlling were combined and a novel flow sensing and controlling system was designed for use in smart factories. The proposed system can sense flow changes using the electrical signals generated by a flapping film; the electrical signals generated are processed using a microcontroller and fed to a controller. The flexible film producing electrical signals using the principle of TENG is called a flapping film triboelectric nanogenerator (FF-TENG). The controller is not fixed and can be modified to adapt to different scenarios by simply adjusting its control strategy. Moreover, the electrical signals generated by the film can be transmitted to the central control room, enabling real-time monitoring and hazard alarms for all aspects of the factory involving flow. This will be of great importance to improve the development of industrial intelligence.

## 2. Structure and working principle of the proposed flow sensing and controlling system

The flow process of a large factory involves many systems, and in Fig. 1, a few common systems are indicated. Fig. 1a (i) displays four FF-TENGs facing different directions and installed on a roof to control the opening and closing of windows automatically, which is more efficient and timely than their manual opening and closing. Fig. 1a (ii) shows a conventional gas–liquid reactor used in a factory. By placing the FF-TENG unit within the gas line and connecting the output of its control system to the gas stirrer, adaptive control can be used to improve the efficiency of the reactions and reduce reactor energy consumption. The adaptive control of the gas flow can also be achieved by connecting the controller output to a valve as shown in Fig. 1a (iii). Fig. 1a (iv) shows the process of air delivery to each room in a central

air conditioning system. The present study uses air conditioning as an example to experiment with the system and to specify the flow control strategy. The ideal room temperature varies from person to person; however, the characteristics of the central air conditioning branch are not controllable. Thus, it is necessary to develop wind-driven devices that can be used in the ventilation ducts of an air distribution system and can be adaptively adjusted to avoid the direct flow of air into a room, causing discomfort to room occupants. The device proposed herein can both sense and control the airflow of the air conditioning system. The essence of the proposed FF-TENG is that it couples a flexible film and a fluid to generate electrical signals. Many studies have already been analysed on the motion of flexible structures, such as flags, used in a fluid flow field [28–33].

Fig. 1b illustrates the structure of the flow sensing and controlling system. The system ensures that irrespective of the wind speed, the length of the flapping film is automatically adjusted to the length that corresponds to the critical flapping state of the film. The first section, measuring 40 mm (width  $W_p$ ) × 40 mm (height  $H_p$ ) × 100 mm (length  $L_p$ ) in size and containing polylactic acid, is mainly used to adjust the film position. It has a slit, approximately 2 mm in height, running through both sides of it. A metal bar holding one end of a fluorinated ethylene propylene (FEP) film treated on both sides (TD-FEP film) moves inside the slit. The second section is an acrylic chamber, measuring 40 mm (width  $W_a$ ) × 40 mm (height  $H_a$ ) × 100 mm (length  $L_a$ ) in size. The top and bottom ends of the acrylic chamber are each covered with a 0.03 mm thick copper electrode layer. At the junction of the two chamber cavities, two jigs, each measuring 40 mm (width  $W_f$ ) × 2 mm (height  $H_f$ ) × 5 mm (length  $L_f$ ) in size, are installed at an upper and lower spacing of 2 mm. The jig divide the whole film into two zones: no flapping and free flapping zones. As the metal bar moves, the ratio of the two zone areas is changed, thereby changing the length of the flapping zone. The control flow chart of the proposed system is shown in Fig. 1c. The system can observe the fluid flow field and control it. When the

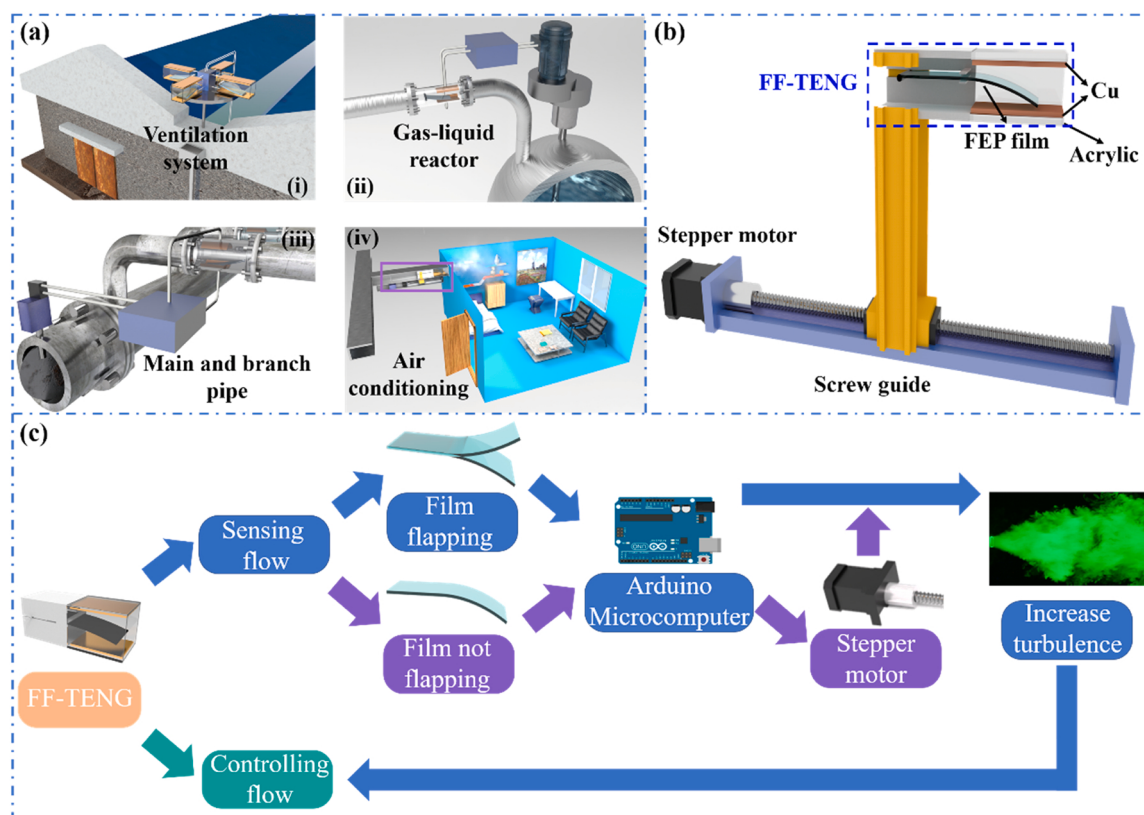


Fig. 1. Applications and the structure of the proposed flow sensing and controlling system. (a) Applications, (b) system structure and (c) control flow chart.

proposed system is operating in the flow-sensing mode, as the fluid passes through the FF-TENG, the film flaps to generate a triboelectric signal, which is collected by a microcontroller to control a motor. When the system is operating in the flow-controlling mode, the motor can change the flapping length of the film and control the turbulence degree of the flow field.

The FF-TENG's flapping under wind excitation is typically a forced vibration. The FF-TENG can be approximated as a thin two-dimensional structure with high extensional and low bending rigidities, satisfying the Euler–Bernoulli beam equation [34].

$$m\ddot{\omega} + D\dot{\omega}^2 - \Delta p = 0 \quad (1)$$

where  $m$  is the mass per unit area,  $D$  is the non-dimensional bending stiffness of the structure,  $\omega$  is the displacement of the FF-TENG along the  $Z$  coordinate and  $\Delta p$  is the wave-induced difference in the air pressure, which is induced across the structure by waves. Among the parameters used in the equation,  $D$  governs the vibration of the thin two-dimensional structure (e.g. FF-TENG).  $D$  is defined as follows:

$$D = \frac{Eh^3}{12(1 - \nu^2)\rho_f U^2 L^3} \quad (2)$$

where  $\nu$  is the Poisson's ratio,  $\rho_f$  is the fluid density,  $U$  is the wave velocity,  $h$  is the thickness of the structure,  $L$  is the length of the structure and  $E$  is the Young's modulus. In the case of FF-TENG,  $D$ , which will largely determine the deformation of the FF-TENG, will eventually affect the electrical performance of the FF-TENG. Owing to its relatively low Young's modulus and high electronegativity, FEP was selected as the dielectric material in FF-TENG [35,36]. Eqs. 1 and 2 govern the fluid coupling and structural motion of the FF-TENG.

### 3. Experimental details

#### 3.1. Components of the flow sensing and controlling system

The pictorial circuit diagram of the proposed flow sensing and controlling system is shown in Fig. 2. It consists of an Arduino microcomputer, a 12 V power supply, an A4988 module, a stepper motor, a filament guide, a blower and the FF-TENG. When the microcontroller receives a signal to start the air conditioner, the A4988 module triggers the 12 V stepper motor to move the filament guide. The film, which has been reset, moves outward until it starts flapping under the airflow within the ventilation system. When the microcontroller receives the electrical signal generated by the FF-TENG, it issues a command to stop

the stepper motor.

#### 3.2. Experimental setup

The experimental setup used in the study is shown in Fig. 3. It includes a computer, programmable electrometer, frequency converter, blower, steady flow chamber, hot-wire anemometer, three-dimensional coordinate frame and a data acquisition and control system. Using the LabVIEW program, the computer controls the frequency converter, which in turn controls the blower to generate airflow with a constant flow rate. The blower outlet is connected to the rectifier chamber. The honeycomb grille is installed in the middle of the rectifier chamber in parallel to the mainstream flow. The metal grid is installed near the nozzle outlet. The honeycomb grille can reduce the curling of the jet fluid, while the metal grid can effectively reduce the pulsation of the incoming flow, break the large-scale vortex structures and reduce the influence of the turbulent boundary layer on the jet velocity. Once the air has passed through the honeycomb grille and metal grid, the turbulence of the flow is significantly reduced, stability of the flow state is increased and the experimental measurement accuracy is improved. The hot-wire probe used in the experiment was fixed on the three-dimensional coordinate frame and the flow field could be measured up to  $x/D = 50$ . A programmable electrometer (Keithley Model 6514) was used to measure the electrical output of the FF-TENG.

### 4. Characterising the flow sensing and controlling system

#### 4.1. FF-TENG output characteristics

As shown in Fig. 4a (i)–(iv), the film, subjected to gravity, falls over the bottom electrode. The air flowing through the chamber passes over the film surface and the film periodically flaps up and down because of the pressure difference it experiences. According to the frictional electron sequence of common materials [37], FEP is more frictionally electronegative than copper; therefore, when the TD-FEP film contacts the copper electrode, the TD-FEP film is negatively charged and the copper electrode is positively charged. Free electrons are transferred from the electrode to the film when the film contacts the electrode during its flapping. At any given wind speed, the negative charge in the FEP film is constant and equal to the total of the positive charge in the two copper electrodes. When the negatively charged FEP film moves away from a copper electrode, an electrical potential difference is established between the two electrodes, driving the free electrons from one electrode to the other via an external circuit. Owing to the periodic

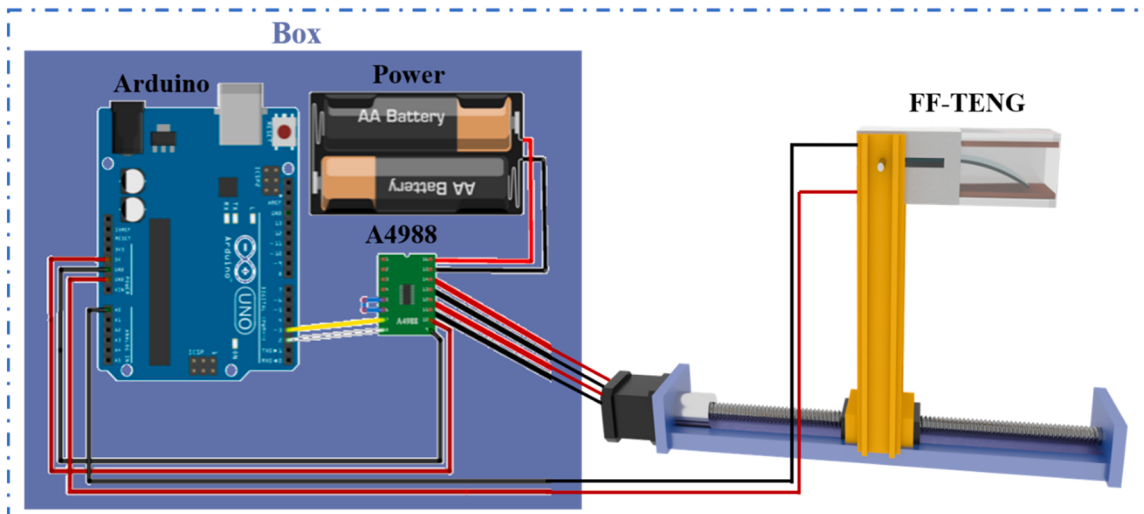


Fig. 2. Pictorial circuit diagram of the flow sensing and controlling system.

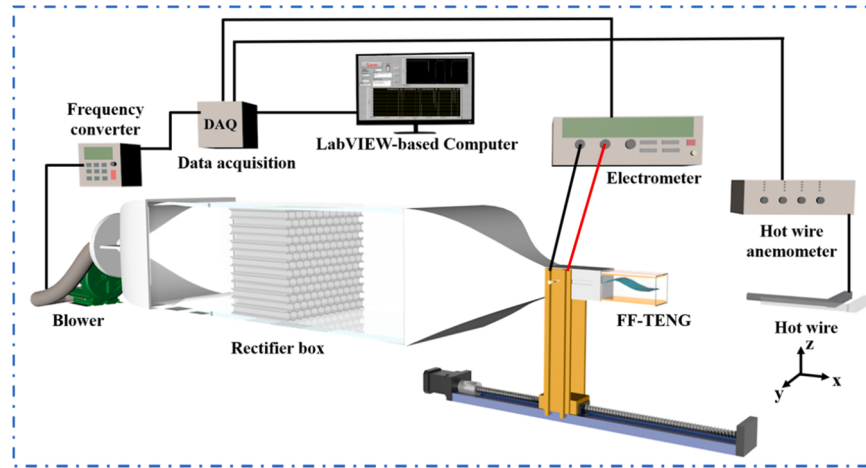


Fig. 3. Experimental setup of the flow sensing and controlling system.

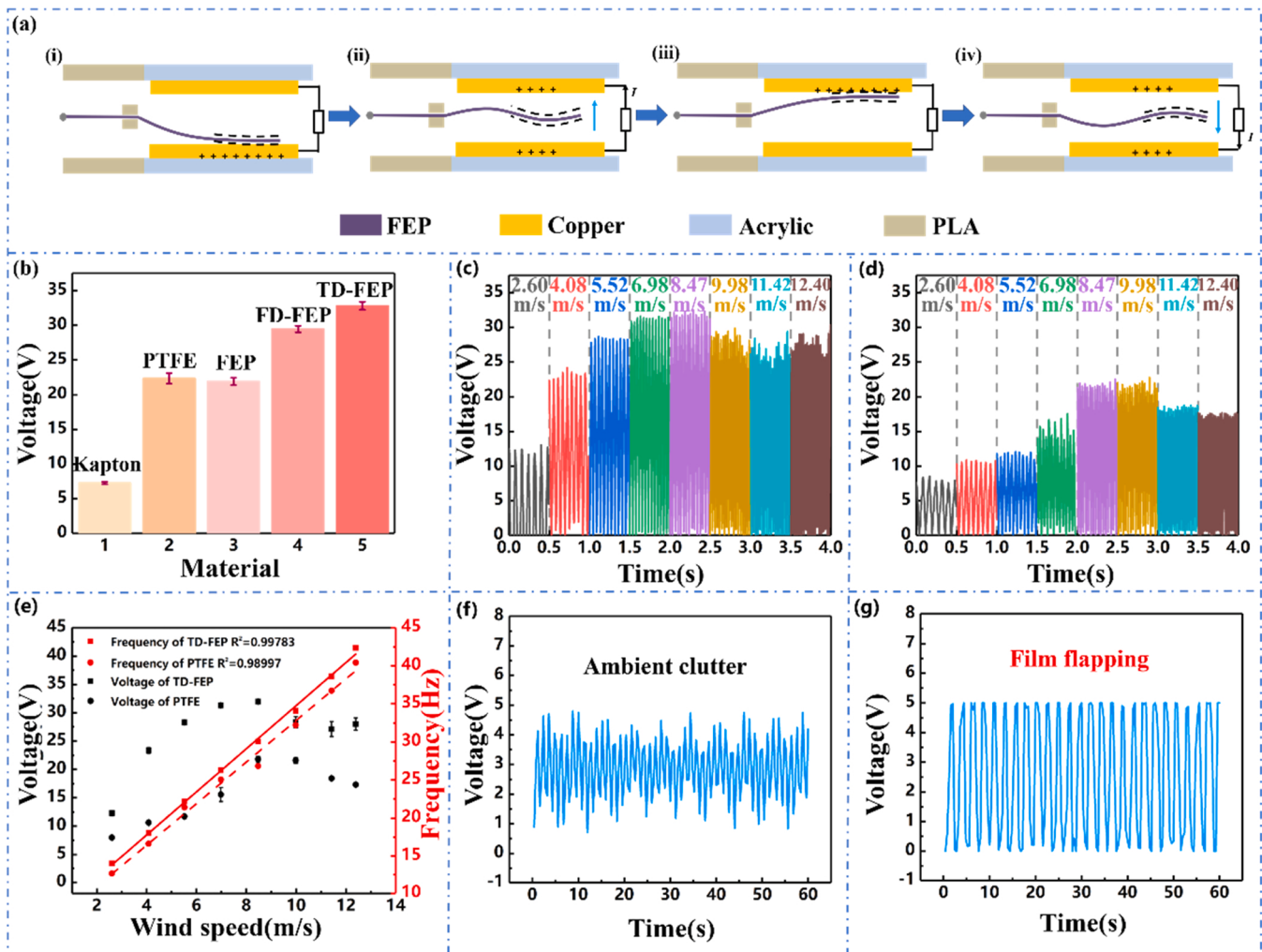


Fig. 4. Electrical output performance of the FF-TENG at a relative humidity between 57% and 64%. (a) Principle of FF-TENG power generation. (b) Kapton, PTFE, FEP, FD-FEP and TD-FEP film output voltages. (c) and (d) TD-FEP film and PTFE membrane output voltages at wind speeds ( $v$ ) between 2.60 and 12.40 m/s. (e) Variations of the TD-FEP film and PTFE membrane output voltage and frequency with wind speed. (f) and (g) Voltage signals generated by ambient clutter and the flapping film.

film flapping caused by the flow, the frequency of the alternating current in the external circuit remains constant and is ultimately captured by the microcontroller to control and regulate the system.

The electrical output performance of FF-TENG was further investigated by placing it at the outlet of a rectangular nozzle at the jet experimental facility. To discuss the effect of different film materials on

the electrical output performance of the FF-TENG, experiments were conducted using Kapton, polytetrafluoroethylene (PTFE), FEP (single-sided), FD-FEP (double-sided FEP without surface treatment) and TD-FEP (double-sided FEP with surface treatment) films. The output voltages and currents of the different films are shown in Fig. 4b and Fig. S1, indicating that TD-FEP film provides the best electrical output performance, which is significantly different from those of the PTFE and single-sided FEP films, with an approximate current of 2  $\mu$ A and an approximate voltage of 32 V. The charge transfer in a single-sided FEP film is less than that in a double-sided FEP film as shown in Figure S2. Moreover, sanding treatment of electrodes increases the number of nanostructures present on the membrane surfaces, increasing the effective contact area of the two electrodes and improving the electrical output performance of the FF-TENG. The scanning electron microscopy images of the untreated and sand-treated surfaces of the double-sided FEP membrane are shown in Fig. S3.

Figs. 4c, 4d and Fig. S4 show the output voltage and current produced by FF-TENG flapping (FD-FEP and PTFE films with a free flapping length of  $2D = 80$  mm) at different wind speeds. As the figures illustrate, the output currents and frequencies of both the FD-FEP and PTFE films increase with increasing wind speed. The output voltages of the FD-FEP and PTFE films first increase and then decrease as the wind speed increases. This phenomenon could be attributed to the chaotic flutter phenomenon and insufficient surface contact of the films at high vibrational frequencies [15]. The sensitivity of the FF-TENG, composed of FD-FEP and PTFE films, to wind speed variations indicate that at low wind speeds ( $v = 2.6\text{--}8.47$  m/s), the output voltage of the FD-FEP film is significantly higher than that of the PTFE film, and the output voltage variation of the FD-FEP film with wind speed is more significant than that of the PTFE film. Thus, an FF-TENG using an FD-FEP film is a better sensor than the one using a PTFE film, which is used to detect air velocity changes in optimised air conditioning ducts where air velocity is

normally in the range of 2–7 m/s. The experimental results also suggest the type of material that can be used in the next stage of implementing automatic and continuous control at different wind speeds. As shown in Fig. 4e, the voltage increases with the wind speed. The frequency of the electrical signal generated by either film varies linearly with wind speed. The TD-FEP curve has a better linearity than the PTFE curve. Although relative humidity has an effect on the electrical output of TENG, the effect is less severe at the relative humidity below 80% [38]. The relative humidity of the air at the air conditioner outlet varies between 55% and 60% [39]. To simulate the relative humidity of the air at the air conditioner outlet, the experiments were conducted at a relative humidity between 57% and 64%.

Fig. 4f shows the spurious voltage signals collected by the serial plotter in the experimental setup. Fig. 4g shows the sinusoidal voltage signals (0–5 V) of the FF-TENG after the film starts flapping. Two voltage thresholds were set for the expected upper and lower voltage signals. When the voltage signals collected five times in a row within a certain time interval exhibit a maximum value exceeding 4.5 V and a minimum value below 0.5 V, the microcontroller realises that the film is flapping and accordingly the adjustment device makes the required adjustment. This method used for determining the signal can effectively remove the interference caused to the microcontroller by environmental noise and improve the accuracy of the film flapping state judgement.

#### 4.2. Flow field performance controlled by the flow sensing and controlling system

The flow fields at  $Re = 8000$  and under six different operating conditions obtained using a smoke generator and a laser sheet light source are shown in Fig. 5a. Panels (i), (ii) and (iii) in Fig. 5a show a simple jet, a jet with a cavity and a jet with a cavity but without a flapping film (NFJ), respectively. Panels (iv), (v) and (vi) in Fig. 5a show a cavity

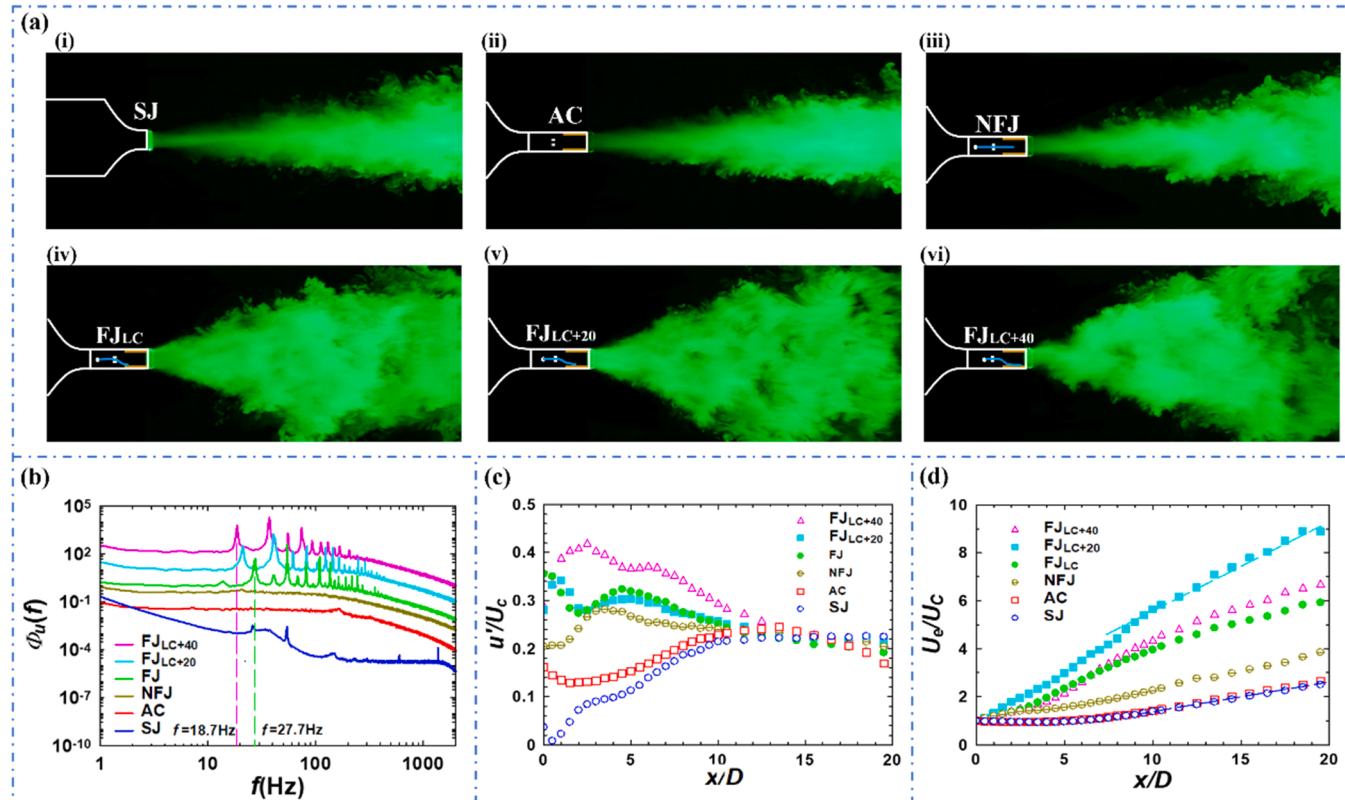


**Fig. 5.** Flow field data plots of the free jet (at  $Re = 8000$ ) and the flapping jet for different flapping lengths of the film during air conditioning. (a) Smoke display plots. (b) Energy spectrum  $\phi_u$  plots for the centre line pulsation velocity  $u$  at the jet exit centre line  $x/D = 1$ . (c) Ratio of the centre line velocity  $U_e$  to the centre line velocity  $U_c$  at different axial positions  $x/D$  along the centre line. (d) Turbulence at different axial positions  $x/D$  along the centre line.

( $F_{LCJ}$ ) with a film length just sufficient for flapping, a cavity with a film length exceeding  $F_{LCJ}$  by 20 mm ( $F_{LC+20J}$ ) and a cavity with the film length exceeding  $F_{LCJ}$  by 40 mm ( $F_{LC+40J}$ ), respectively. As shown in Fig. 5a and Supplementary Movie 1, the diffusion angle of the oscillating jet observed in the presence of a flapping film is significantly larger than that observed in the absence of a flapping film. ‘Hollow’ areas are visible in the smoke of the flapping jet, the surrounding air is drawn into the main body of the jet. The presence of these areas indicates the strong coiling and mixing ability of the film-induced flapping jet.

To gain a thorough understanding about how flow field characteristics can vary, six flow fields along the centre line of the jet outlet were measured using a hot-wire anemometer for  $x/D$  between 0 and 20. Fig. 5b shows the frequency spectra for the six cases at a distance of approximately  $x/D = 1$  from the centre of the jet exit. From the spectra, it can be seen that the jet induced by film flapping has a clear periodicity attaining its maximum frequency when the film just starts to flap. The highest oscillation frequency of the jet is approximately 27.7 Hz, and the flapping frequency decreases as the film length increases. Fig. 5c shows the centre line velocity decay rate of the flow field at the centre line; the slope of the graph of velocity ratio  $U_e/U_c$  vs.  $x/D$  reflects how quickly the velocity decays downstream from the jet outlet, where  $U_c$  and  $U_e$  represent the local centre line mean velocity and the nozzle outlet mean velocity, respectively. Compared with the free jet, the decay rate of the centre line velocity in the flapping jet increases significantly. Because the ambient fluid velocity is almost zero, the faster the velocity decay is,

the higher will be the quantity of ambient fluid drawn into the main body of the jet and blended, thus improving the blending effect. The figure also shows that during film flapping, the fluid velocity decays to less than 20% of the outlet fluid velocity at  $20H$  downstream; therefore, the installation of the proposed device at the air conditioning system outlet will significantly eliminate the discomfort caused by air flowing directly into rooms.

The variation in the fluid turbulence in the six cases shown in Fig. 5d also shows that the velocity pulsation of the flapping jet is considerably high and that the greater the turbulence is, the easier it is for the jet to mix with the ambient fluid at the molecular level and transfer heat more quickly and adequately. The turbulence in NFJ is smaller than that with the flapping jet and greater than those in the two cases in which the film does not flap. However, the small flapping phenomenon also increases the velocity pulsation of the flapping jet. Analysis of the flow fields of the six cases reveals that the oscillatory motion induced by the flapping film significantly enhances the ability of the jet to reel in and mix with the ambient fluid.

#### 4.3. Demonstration of the flow sensing and controlling system

To observe the changes in the electrical signals produced in the proposed flow sensing and controlling system during the regulation process, the voltage signals collected by the microcontroller were displayed in real time using a serial plotter. As shown in Fig. 6a and

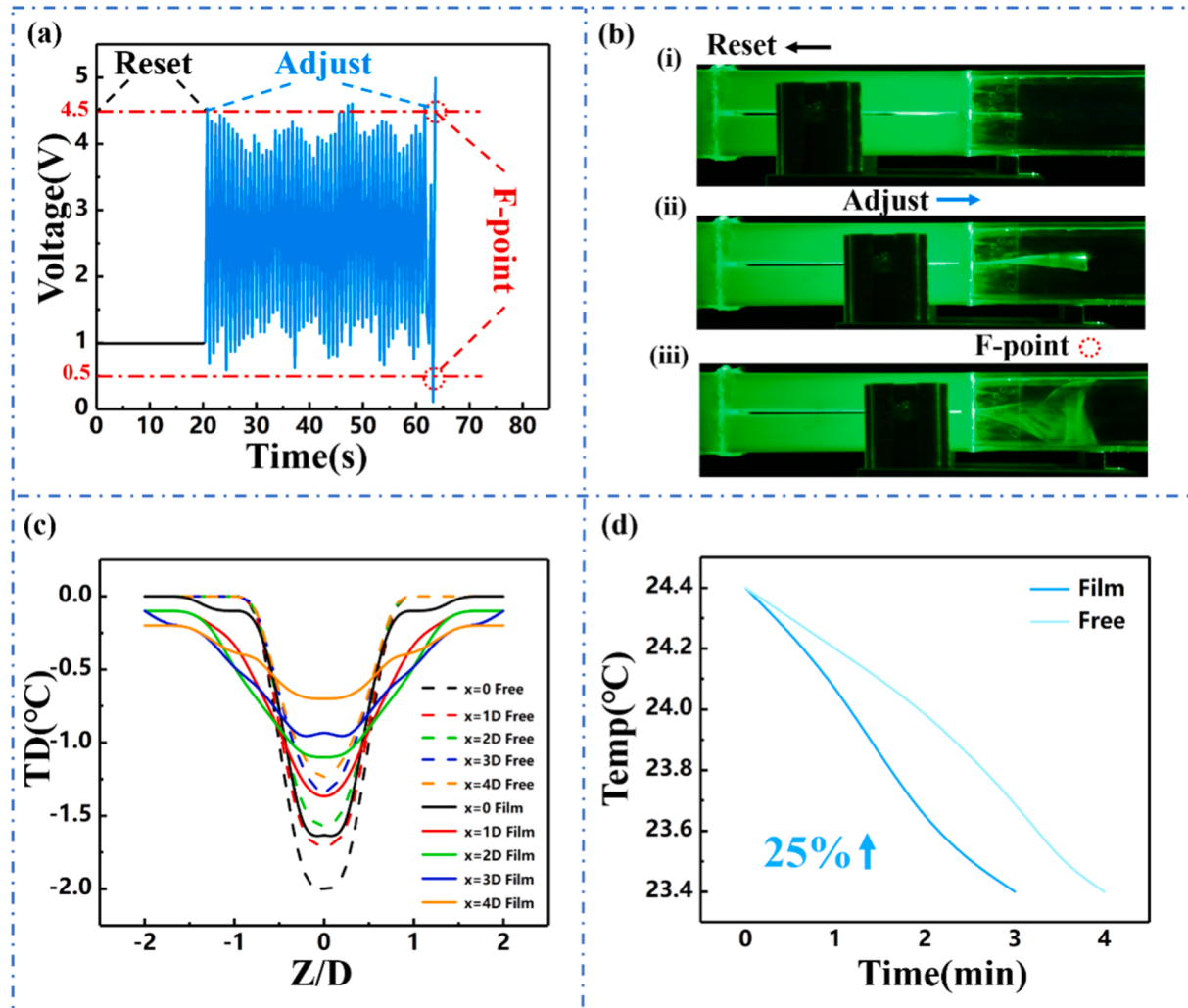


Fig. 6. Regulation process and cooling effect of the flow sensing and controlling system. (a) Voltage variation with time during the regulation process. (b) State of the film during the regulation process. (c) Effect of the system on the cooling space and (d) effect of the system on the cooling rate.

Supplementary Movie 2, the entire adjustment process can be divided into three processes. The first process is the initialisation phase. When the airflow speed changes, the system has to be re-adjusted to return to the critical flapping state. In this phase, the device is restored to its initial state. At this point, although the film is not flapping, a voltage signal of approximately 1 V can still be observed because of the charging that occurred when the film flapped against the upper and lower electrodes before the initialisation phase. The charge will not disappear immediately. The second process is the adjustment process, which involves adjustment of the device so that the film is positioned in such a way that it can just start flapping. At this point, the flapping length of the film gradually increases although the film will not flap and the voltage signal collected by the microcontroller becomes mainly an interference signal. The third process is the stopping of the adjustment process. At this time, the device has reached the state where the film is about to flap. The microcontroller collects the electrical signal generated by the friction between the film and the upper and lower copper electrodes, immediately commands the stepping motor to stop the rotation and the film is fixed at the required position to optimise the wind distribution effect. The difference in the two voltage measurements is due to the differences in the instruments used. The actual sensing and controlling is done through Arduino, and the maximum voltage that can be measured at the serial port of Arduino is 5 V. Because the device has to determine whether the film is in the flapping state or not, Arduino uses voltage division to measure the voltage. As shown in Fig. 6b, the film states corresponding to the three adjustment processes are displayed using a laser that works with a high-speed camera (EOS 5D Mark iii). The length of the film inside the acrylic chamber gradually increases during the adjustment process, and chattering can be clearly seen when the length of the film attains a certain value (Fig. 6b (ii)); however, the film does not reach a stable flapping state. As the length of the film continues to increase, high frequency flapping suddenly begins, and the critical flapping state occurs at F-point as shown in Fig. 6b (iii).

To investigate the effect of the proposed flow sensing and controlling system on the air distribution range of the outlet, temperature variations in the  $x$ - $z$  plane in which the centre line was located were measured using a temperature sensor at the nozzle outlet as shown in Figure S5. Measurements were made for different flow field positions in the  $z$ -direction for  $x = 0, 1D, 2D, 3D$  and  $4D$  ( $D = 40$  mm). The difference between the temperature at the point of observation and room temperature (TD) is shown in Fig. 6c. As shown in the figure, compared with the cooling range of a conventional free jet, the cooling range of the proposed system is significantly wide due to the flapping film, which can effectively reduce the blowing of direct air. The cooling effect is strongest at  $x = 4H$  with a maximum temperature drop of  $0.5^\circ\text{C}$ . The effect of the flow sensing and controlling system on the rate of temperature drop is shown in Fig. 6d. Compared with a conventional free jet, the proposed flow sensing and controlling system shortened the time taken for the temperature to drop from  $24.4^\circ\text{C}$  to  $23.4^\circ\text{C}$  within 1 min at the same nozzle exit position. Furthermore, the cooling rate can be increased by approximately 25% by using the proposed system. Thus, the proposed system can play an important role in optimising the air distribution of air conditioning systems.

## 5. Conclusions

A novel flow sensing and controlling system based on the FF-TENG was designed for smart factories. The device can sense the fluid flow state and adjust the industrial processes of applications, such as ventilation systems, gas–liquid reactors, airflow control valves and air distribution systems, to ultimately control the flow field. Herein, the usage of the proposed flow sensing and controlling system was investigated in an air distribution system. The conclusions of the study are as follows.

- (1) Among the five materials studied, the TD-FEP film was found to produce the highest electrical output performance and was sensitive to changes in wind speed, particularly low wind speeds.
- (2) The frequency of the electrical signal, a sinusoidal signal between 0 and 5 V, generated by the FF-TENG increases linearly with wind speed.
- (3) After setting the voltage threshold and determining the voltage signal required to remove environmental clutter, the film can be kept in the state of constant flapping using a single chip microcomputer.
- (4) The experiments conducted at  $Re = 8000$  ( $v = 4.47$  m/s) show that FF-TENG can effectively expand the range of cooling space and accelerate the cooling rate by 25%.

## CRediT authorship contribution statement

**Xiangyi Wang:** Conceptualization, Methodology, Software. **Chuanqing Zhu:** Data curation, Writing – original draft preparation; **Mengwei Wu:** Formal analysis, Data curation. **Jialin Zhang:** Software. **Pengfei Chen:** Validation. **Hao Chen:** Validation. **Chenxing Jia:** Data curation. **Xiao Liang:** Data curation. **Minyi Xu:** Supervision, Writing – review & editing.

## Declaration of Competing Interest

The authors declare that they have no known competing financial interests or personal relationships that could have appeared to influence the work reported in this paper.

## Acknowledgement

The authors are grateful for the support from Dalian Outstanding Young Scientific and Technological Talents Project (2021RJ11).

## Appendix A. Supporting information

Supplementary data associated with this article can be found in the online version at doi:[10.1016/j.sna.2022.113727](https://doi.org/10.1016/j.sna.2022.113727).

## References

- [1] V. Paelke, Augmented reality in the smart factory: Supporting workers in an industry 4.0. environment, Proceedings of the 2014 IEEE Emerging Technology and Factory Automation (ETFA), vol. 1, no. 1, Sep. 2014, doi: [10.1109/etfa.2014.7005252](https://doi.org/10.1109/etfa.2014.7005252).
- [2] L. Li, China's manufacturing locus in 2025: With a comparison of 'Made-in-China 2025' and 'Industry 4.0', Technol. Forecast. Soc. Change 135 (2) (2018) 66–74, <https://doi.org/10.1016/j.techfore.2017.05.028>.
- [3] L. Feng, C. Zhao, B. Huang, Adversarial smoothing tri-regression for robust semi-supervised industrial soft sensor, J. Process Control 108 (2021) 86–97.
- [4] V. Chang, C. Martin, An industrial IoT sensor system for high-temperature measurement, Comput. Electr. Eng. (2021) 95.
- [5] L. Franz, U. Markus, P. Victor, Translational sensor technology: from laboratory to industrial environments. Reference Module in Biomedical Sciences, 2022.
- [6] N. Afsharimanesh, A. Nag, M.E.E. Alahi, T. Han, S.C. Mukhopadhyay, Interdigital sensors: biomedical, environmental and industrial applications, Sens. Actuators A Phys. (2020) 305.
- [7] C. Zhao, F. Wang, Z. Mao, N. Lu, M. Jia, Quality prediction based on phase-specific average trajectory for batch processes, AIChE J. 54 (3) (2008) 693–705.
- [8] R. Aversa, R.V.V. Petrescu, F.I.T. Petrescu, A. Apicella, Smart-factory: optimization and process control of composite centrifuged pipes, Am. J. Appl. Sci. 13 (11) (2016) 1330–1341, <https://doi.org/10.3844/ajassp.2016.1330.1341>.
- [9] Z.L. Wang, On Maxwell's displacement current for energy and sensors: the origin of nanogenerators, Mater. Today 20 (2) (2017) 74–82, <https://doi.org/10.1016/j.mattod.2016.12.001>.
- [10] Z.L. Wang, On the first principle theory of nanogenerators from Maxwell's equations, Nano Energy 68 (5) (2020), 104272, <https://doi.org/10.1016/j.nanoen.2019.104272>.
- [11] F. Xi, et al., Self-powered intelligent buoy system by water wave energy for sustainable and autonomous wireless sensing and data transmission, Nano Energy 61 (6) (2019) 1–9, <https://doi.org/10.1016/j.nanoen.2019.04.026>.

- [12] J. An, et al., Reliable mechatronic indicator for self-powered liquid sensing toward smart manufacture and safe transportation, *Mater. Today* 41 (7) (2020) 10–20, <https://doi.org/10.1016/j.mattod.2020.06.003>.
- [13] Z. Wang, P. Fei, H. Xiong, C. Qin, W. Zhao, X. Liu, CoFe2O4 nanoplates synthesized by dealloying method as high performance Li-ion battery anodes, *Electrochim. Acta* 252 (8) (2017) 295–305, <https://doi.org/10.1016/j.electacta.2017.08.189>.
- [14] X. Xiao, et al., Honeycomb structure inspired triboelectric nanogenerator for highly effective vibration energy harvesting and self-powered engine condition monitoring, *Adv. Energy Mater.* 9 (40) (2019), 1902460, <https://doi.org/10.1002/aenm.201902460>.
- [15] J. Bae, et al., Flutter-driven triboelectrification for harvesting wind energy, *Nat. Commun.* 5 (1) (2014), <https://doi.org/10.1038/ncomms5929>.
- [16] Z. Quan, C.B. Han, T. Jiang, Z.L. Wang, Wind energy: robust thin films-based triboelectric nanogenerator arrays for harvesting bidirectional wind energy, *Adv. Energy Mater.* 6 (5) (2016), <https://doi.org/10.1002/aenm.201670031>.
- [17] H. Phan, et al., Aerodynamic and aeroelastic flutters driven triboelectric nanogenerators for harvesting broadband airflow energy, *Nano Energy* 33 (12) (2017) 476–484, <https://doi.org/10.1016/j.nanoen.2017.02.005>.
- [18] Y. Yang, et al., Triboelectric nanogenerator for harvesting wind energy and as self-powered wind vector sensor system, *ACS Nano* 7 (10) (2013) 9461–9468, <https://doi.org/10.1021/nn4043157>.
- [19] H. Guo, et al., A nanogenerator for harvesting airflow energy and light energy, *J. Mater. Chem. A* 2 (7) (2014) 2079–2087, <https://doi.org/10.1039/c3ta14421f>.
- [20] S. Wang, X. Mu, X. Wang, A.Y. Gu, Z.L. Wang, Y. Yang, Elasto-aerodynamics-driven triboelectric nanogenerator for scavenging air-flow energy, *ACS Nano* 9 (10) (2015) 9554–9563, <https://doi.org/10.1021/acsnano.5b04396>.
- [21] M. Xu, et al., An aeroelastic flutter based triboelectric nanogenerator as a self-powered active wind speed sensor in harsh environment, *Extrem. Mech. Lett.* 15 (16) (2017) 122–129, <https://doi.org/10.1016/j.eml.2017.07.005>.
- [22] Y. Wang, et al., A novel humidity resisting and wind direction adapting flag-type triboelectric nanogenerator for wind energy harvesting and speed sensing, *Nano Energy* 78 (17) (2020), 105279, <https://doi.org/10.1016/j.nanoen.2020.105279>.
- [23] Q. Xu, Y. Fang, Q. Jing, N. Hu, K. Lin, Y. Pan, L. Xu, H. Gao, M. Yuan, L. Chu, Y. Ma, Y. Xie, J. Chen, L. Wang, A portable triboelectric spirometer for wireless pulmonary function monitoring, *Biosens. Bioelectron.* 187 (2021), 113329.
- [24] Q. Xu, Y. Lu, S. Zhao, N. Hu, Y. Jiang, H. Li, Y. Wang, H. Gao, Y. Li, M. Yuan, L. Chu, J. Li, Y. Xie, A wind vector detecting system based on triboelectric and photoelectric sensors for simultaneously monitoring wind speed and direction, *Nano Energy* (2021) 89.
- [25] M. Xu, M. Wu, J. Mi, A new type of self-excited flapping jets due to a flexible film at the nozzle exit, *Exp. Therm. Fluid Sci.* 106 (18) (2019) 226–233, <https://doi.org/10.1016/j.expthermflusci.2019.04.031>.
- [26] M. Wu, M. Xu, J. Mi, R.C. Deo, Mixing characteristics of a film-exciting flapping jet, *Int. J. Heat Fluid Flow* 82 (19) (2020), 108532, <https://doi.org/10.1016/j.ijheatfluidflow.2019.108532>.
- [27] M. Wu, C. Li, C. Zhu, G. Wang, M. Xu, J. Mi, On flapping jets induced by a fluttering film and from circular nozzles of smooth contraction, orifice plate and long pipe, *Exp. Fluids* 63 (2022) 5.
- [28] B. Chun-Yu, T. Chao, Y. Xie-Zhen, L. Xi-Yun, Flutter of finite-span flexible plates in uniform flow, *Chin. Phys. Lett.* 27 (6) (2010), 064601, <https://doi.org/10.1088/0256-307x/27/6/064601>.
- [29] M. Argentina, L. Mahadevan, Fluid-flow-induced flutter of a flag, *Proc. Natl. Acad. Sci. USA* 102 (6) (2005) 1829–1834, <https://doi.org/10.1073/pnas.0408383102>.
- [30] F. Liu, J. Cai, Y. Zhu, H.M. Tsai, A.S.F. Wong, Calculation of wing flutter by a coupled fluid-structure method, *J. Aircr.* 38 (2) (2001) 334–342, <https://doi.org/10.2514/2.2766>.
- [31] Z. Pang, L. Jia, X. Yin, Flutter instability of rectangle and trapezoid flags in uniform flow, *Phys. Fluids* 22 (12) (2010), 121701, <https://doi.org/10.1063/1.3525920>.
- [32] L. Schoueiler, C. Eloy, Coupled flutter of parallel plates, *Phys. Fluids* 21 (8) (2009), 081703, <https://doi.org/10.1063/1.3204672>.
- [33] M.J. Shelley, J. Zhang, Flapping and bending bodies interacting with fluid flows, *Annu. Rev. Fluid Mech.* 43 (1) (2011) 449–465, <https://doi.org/10.1146/annurev-fluid-121108-145456>.
- [34] C. Eloy, R. Lagrange, C. Souilliez, L. Schoueiler, Aeroelastic instability of cantilevered flexible plates in uniform flow, *J. Fluid Mech.* 611 (2008) 97–106.
- [35] Z.L. Wang, Triboelectric nanogenerators as new energy technology for self-powered systems and as active mechanical and chemical sensors, *ACS Nano* 7 (11) (2013) 9533–9557.
- [36] Z.L. Wang, A.C. Wang, On the origin of contact-electrification, *Mater. Today* 30 (2019) 34–51.
- [37] D.K. Davies, Charge generation on dielectric surfaces, *J. Phys. D Appl. Phys.* 2 (11) (1969) 1533–1537, <https://doi.org/10.1088/0022-3727/2/11/307>.
- [38] H. Guo, J. Chen, L. Tian, Q. Leng, Y. Xi, C. Hu, Airflow-induced triboelectric nanogenerator as a self-powered sensor for detecting humidity and airflow rate, *ACS Appl. Mater. Interfaces* 6 (19) (2014) 17184–17189.
- [39] R. Niu, Y. Fan, L. Geng, Adaptability of a temperature and humidity independent control air-conditioning system in green office buildings, *J. Build. Eng.* (2021) 42.

**Xiangyi Wang** received his undergraduate degree from Dalian Maritime University, China, in 2021, and his major is Marine Engineering, and now he is a graduate student in Beijing Institute of Nanoenergy and Nanosystems, Chinese Academy of Sciences, China. His research interests are focused on blue energy harvesting by using triboelectric nanogenerator

**Chuanqing Zhu** is currently pursuing his doctor degree in Dalian Maritime University, China. His current research interests include blue energy, self-powered systems, and triboelectric nanogenerators.

**Mengwei Wu** received his B.S. degree from Dalian Maritime University in Dalian, China, in 2019. He is working toward the Ph.D. degree in Peking University in Beijing, China. His current research interests include turbulence, experimental fluid mechanics and triboelectric nanogenerators.

**Jialin Zhang**, Dalian Maritime University is an undergraduate. His current main research interests are experimental fluid mechanics and triboelectric nanogenerators.

**Pengfei Chen** received his bachelor's degree at Dalian Maritime University in 2018. Now he is a doctoral candidate in Beijing Institute of Nanoenergy and Nanosystem, Chinese Academy of Science. His research interests are focused on blue energy harvesting and self-powered sensor of high-performance, high-durability TENG.

**Hao Chen** is currently pursuing a bachelor's degree in Dalian Maritime University, China. His current research interests include turbulent jets, flow-induced vibration, and triboelectric nanogenerators.

**Chenxing Jia** has been studying mathematics as an undergraduate in Dalian Maritime University since 2019. Her current research interests involve neural networks and deep learning.

**Xiao Liang** is currently pursuing his bachelor's degree in Dalian Maritime University, China. His current research interest is turbulent jets.

**Minyi Xu** received his Ph.D. degree from Peking University in 2012. During 2016–2017, he joined Professor Zhong Lin Wang' group at Georgia Institute of Technology. Now he is a Professor in the Marine Engineering College, Dalian Maritime University. His current research is mainly focused on the areas of blue energy, self-powered systems, triboelectric nanogenerators and its practical applications in smart ship and ocean.